
# Macro- and micro-mechanical behaviour of a γ′ strengthened Ni-based superalloy at cryogenic temperatures

Materials & Design 209 (2021) 109954

Contents lists available at ScienceDirect

Materials & Design

journal homepage: www.elsevier.com/locate/matdes

# Macro- and micro-mechanical behaviour of a $\gamma'$ strengthened Ni-based superalloy at cryogenic temperatures

Nitesh Raj Jaladurgam [a], Saurabh Kabra [b], Magnus Hörnqvist Colliander [a,*]

[a] Chalmers University of Technology, Department of Physics, SE-41296 Gothenburg, Sweden
[b] ISIS Facility, Rutherford Appleton Laboratory, Didcot OX11 0QX, UK

## HIGHLIGHTS

- Load distribution in a $\gamma'$ strengthened superalloy is measure by in-situ neutron diffraction.
- The effect of particle size on Load distribution at cryogenic temperatures is studied.
- Co-deformation of phases leads to intergranular load transfer between in matrix.
- Coarse $\gamma'$ microstructure experience both intergranular and intragranular load transfer.
- Coarse particles initially behave elastically but yield at higher stresses.

## GRAPHICAL ABSTRACT

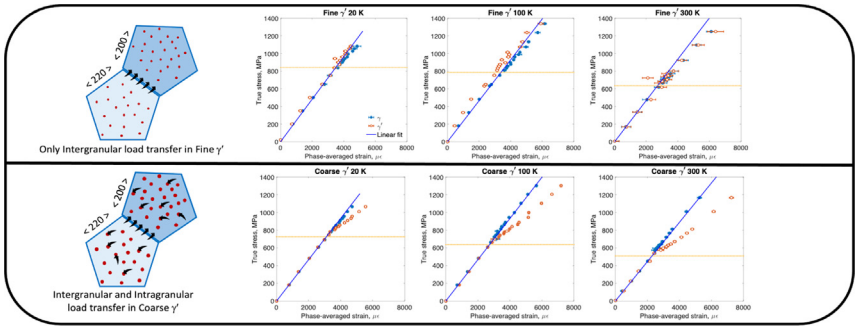


## ARTICLE INFO

*Article history:*
Received 4 May 2021
Revised 15 June 2021
Accepted 2 July 2021
Available online 08 July 2021

*Keywords:*
Load re-distribution
Ni-base superalloy
Cryogenic temperatures
Phase-specific response
In-situ neutron diffraction

## ABSTRACT

In-situ neutron diffraction was performed during tensile deformation of a Ni-based superalloy, Haynes 282, at 20, 100 and 300 K. Two distinct uni-modal microstructures with fine (20 nm) and coarse (200 nm) $\gamma'$ particles were investigated. On the macro-scale yield strength increased and ductility decreased with decreasing temperature, although the most significant decrease in ductility occurred between 100 and 20 K. The work hardening differed between the two microstructures, but was independent of temperature for each microstructure. On the micro-scale intergranular elastic interactions mainly lead to a transfer of the load to grains with the ⟨200⟩ orientation parallel to the tensile axis. No further load re-distribution between matrix and particles occurred in the microstructure with fine $\gamma'$, where shearing of precipitates lead to co-deformation at all temperatures. In the coarse $\gamma'$ microstructure, the load was transferred intragranularly from matrix to particles, in addition to the intergranular load transfer. The particles initially behaved elastically while the matrix deformed plastically, but at higher stresses a change in load partitioning indicated that also the $\gamma'$ phase underwent plastic deformation as a result of the stress build-up from the load partitioning. The tendency for, and effect of, plastic deformation of $\gamma'$ increased with decreasing temperature.



## 1. Introduction

Ni-based superalloys is an important class of structural materials used in challenging high temperature applications in aerospace and energy sectors where a combination of high microstructure stability, strength and resistance to creep, fatigue and oxidation is required [1]. The mechanical properties depend critically on the deformation mechanisms, and Ni-base superalloys are known to exhibit transitions between different mechanisms depending on loading condition and temperature. Slip-mode transition [2], twinning during intermediate temperature creep [3–6] and

* Corresponding author.
*E-mail address:* magnus.colliander@chalmers.se (M.H. Colliander).

https://doi.org/10.1016/j.matdes.2021.109954
0264-1275/

thermomechanical fatigue loading [7–9], temperature dependent dislocation coupling [10,11], and microstructure-dependent load partitioning between matrix and strengthening phases [12–14] have all been reported. The effects of such transitions on the phase-specific mechanical response in precipitation strengthened alloys have been previously investigated using in situ neutron diffraction, where e.g. octahedral-to-cube slip could be directly measured [2].

Furthermore, as they retain, or even improve, many critical properties such as toughness and ductility [15] and fatigue resistance [16–18] at cryogenic temperatures, they have found extensive applications in e.g. aerospace applications [19,20] and superconducting magnet systems, e.g. for use in the International Thermonuclear Energy Reactor (ITER) [21]. At cryogenic temperatures, several superalloys have been reported to undergo extensive micro-twinning, which can lead to ductility levels being higher than at room temperature [22–24]. However, while there are several reports of strength, ductility, fatigue properties etc (see e.g. [25] for a compilation of cryogenic mechanical data), there is a lack of studies regarding phase-specific response in order to fully understand the deformation process at these temperatures. In particular, the well known effect of strengthening particle size on the load transfer between $\gamma$ and $\gamma'$ in these alloys, has not been previously investigated at sub-zero temperatures.

Here we report the first study of load partitioning in a $\gamma'$ strengthened Ni-base superalloy at cryogenic temperatures. The relatively recent alloy Haynes 282 in two different heat treatment conditions was subjected to tensile testing at 20, 100 and 300 K, and the phase and orientation-specific mechanical response was recorded by in situ neutron diffraction. The results shows complex temperature dependent interactions involving both intergranular (between grains with different orientation) and intragranular (between phases in each grain) load transfer.

## 2. Experimental

Haynes 282 is a relatively recently introduced $\gamma'$ ($L1_2$, $Ni_3(Ti,Al)$) strengthened Ni-based superalloy, specifically developed in order to have better weldability than similar alloys [26], which could make it interesting for cryogenic applications such as pressure vessels. The nominal composition is (in wt.%) 19.52Cr-10.33Co-8.56 Mo-2.13Ti-1.52Al with a balance of Ni and other elements such as Fe, B, P, S and Si in minor amounts. The average grain size was 150 $\mu$m and texture was random. Tensile samples with a diameter of 6 mm and gauge length of 30 mm were machined from forged bars. The samples were subjected to a solution treatment at 1120 °C for 30 min followed by either (a) water quenching, carbide stabilization at 1010 °C for 1 h and ageing at 788 °C for 8 h; or (b) furnace cooling to 950 °C, ageing at 950 °C for 30 min followed by slow cooling (~0.1 °C $min^{-1}$) to 500 °C and then water quenching. Further details are given in [14]. Heat treatment (a) resulted in a uni-modal $\gamma'$ distribution with an average size around 20 nm (hereafter denote as *fine* $\gamma'$), whereas heat treatment (b) produce a nearly uni-modal $\gamma'$ distribution with an average size of around 200 nm (*coarse* $\gamma'$). The volume fraction of precipitates was approximately the same in both cases, around 0.2. In the coarse microstructure smaller secondary $\gamma'$ particles were occasionally seen, but the fraction was very low, and these particles are assumed not to influence the mechanical behaviour. The heat treatments did not affect the grain size of the material. The heat treated samples were subjected to in situ neutron diffraction during tensile testing at the time-of-flight (TOF) engineering diffractometer Engin-X [27] located at ISIS Neutron and Muon Source, UK, following the methodology described in reference [14]. Full diffractograms were collected with the scattering vector (measured strain direction) in the tensile direction using a $4\times4\times4$ $mm^3$ gauge volume and acquisition times of around one hour per data point. Tests were performed at room temperature in air as well as at cryogenic temperatures 20 and 100 K in vacuum by using a dedicated chamber [28] which enables diffraction measurements during deformation [29–32]. Note that the room temperature data was derived from the same data set as used in [14]. Representative diffractograms from the unloaded state at each temperature are shown in Fig. S1 in the supplementary material. Single peak fits in GSAS-II [33] was used to obtain interplanar $d$-spacing from the different peaks as a function of applied stress, which allowed subsequent calculation of orientation specific elastic lattice strains according to $\epsilon_{hkl}(\sigma) = d_{hkl}(\sigma)/d^0_{hkl} - 1$, where $d^0_{hkl}$ and $d_{hkl}$ are the $d$-spacings of the ($hkl$) peak measured in the unloaded state and at applied stress $\sigma$, respectively. As the phases are coherent, the fundamental peaks consist of contributions from both $\gamma$ and $\gamma'$, and require deconvolution using information from fitting of the corresponding superlattice peaks. This can only be done for the (200) and (220) doublets, as there are no superlattice peaks corresponding to (111) and (311). However, as we have previously shown that the effect of deconvolution on the $\gamma$ $d$-spacings is negligible for the material and microstructures investigated here [14], we consider the undeconvoluted fits of (111) and (311) peaks to be representative of the behaviour of their respective orientations in the $\gamma$ phase. Deconvolution of the (200) and (220) peaks was facilitated by fixing the $d$-spacing of the $\gamma'$ contribution based on the fit of the corresponding superlattice peak, i.e. $d^{\gamma'}_{200} = 1/2d^{\gamma'}_{100}$ and $d^{\gamma'}_{220} = 1/2d^{\gamma'}_{110}$. In the subsequent refinements of the doublet peak the intensity, position and width of the $\gamma$ contribution were refined, whereas only intensity and width (without further constraints) were refined for $\gamma'$. This approach was previously shown to give consistent results for the particular alloy [14], where the validity of the convolution is further discussed. Examples of doublet peak fits are shown in Fig. S2 in the supplementary material. Phase-averaged lattice strains were subsequently calculated by averaging the orientation-specific values, weighted for multiplicity [34]. During the cooling to 20 K diffractograms were also collected from coarse $\gamma'$ samples at selected temperatures inorder to measure the coefficient of thermal expansion (CTE) and the constrained lattice misfit. Similar measurements were not made for the fine $\gamma'$ microstructure due to the large uncertainties associated with the low intensity of the superlattice peaks.

## 3. Results and discussion

### 3.1. Thermal expansion and lattice misfit

To determine the CTE, $\alpha$, and lattice misfit, $\delta$, lattice parameters determined as the average of the (100) and (110) superlattice peaks for $\gamma'$, and the average of the decomposed (200) and (220) peaks for $\gamma$, were used. The lattice parameters were measured from two different samples, denoted S1 and S2. S1 was measured at 300, 200, 100 and 20 K, whereas S2 was measured at 250, 150 and 20 K. As can be seen from Fig. 1, where the lattice parameters from S1 and S2 are plotted against temperature, there is a small but systematic difference in $a_\gamma$, where S1 appears to show slightly larger values. This is likely caused by a small difference in residual intragranular stresses between the two sample, which becomes visible as only two peaks are used for lattice parameter estimation. For the CTE calculations we therefore only consider data from S1, which covers the entire temperature range of interest. The lattice parameter of each phase $p$, $a_p$, where fitted with a $2^{nd}$ order polynomial ($a = a_0 + cT^2$, where $a_0$ and $c$ are constants) with respect to temperature, $T$, to calculate the phase-specific CTE, $\alpha_p$, according to

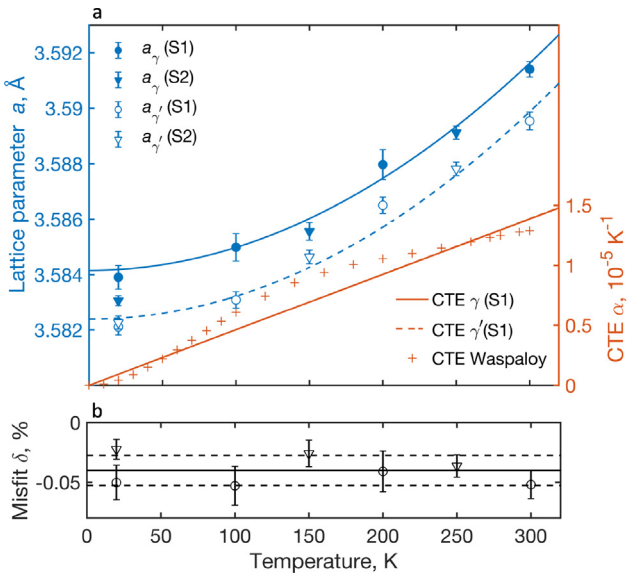


**Fig. 1.** (a) Lattice parameters of $\gamma$ and $\gamma'$, with associated 2$^{nd}$ order polynomial fits, and resulting CTE calculated from Eq. 1. Note that the CTE curves for $\gamma$ and $\gamma'$ overlap, and the curve for $\gamma'$ is hidden behind the curve for $\gamma$. The CTE data for Waspaloy was taken from the values reported for the age-hardened condition in [35]. (b) Lattice misfit calculated according to Eq. 2. The solid and dashed lines represent the average values ± one standard deviation, respectively.

$$\alpha_p(T) = \frac{1}{a_p}\frac{\partial a_p}{\partial T}. \quad (1)$$

The CTE is compared to data measured for Waspaloy [35], which is a relatively similar Ni-base superalloy, in Fig. 1, and excellent agreement can be seen. It should be noted that while the limited number of data points did not allow reliable fitting of more physically suitable models for $a_p(T)$, the agreement shows that literature data for Waspaloy can be safely used to estimate thermal contraction of Haynes 282 at cryogenic temperatures.

The constrained lattice misfit can be calculated from the lattice parameters as

$$\delta = 2\frac{a_{\gamma'} - a_\gamma}{a_{\gamma'} + a_\gamma}. \quad (2)$$

The misfit is essentially independent of temperature, with a small negative average value of $-0.04 \pm 0.01$ % (see Figure 1(b)). This agrees well with the predicted $\gamma/\gamma'$ misfit in Haynes 282 reported in [36] after extrapolation to room temperature, which lies in the range $-0.08$ to $-0.04$ % depending on exact composition within the specification limits. The negative misfit is likely related to the relatively high amount of Mo in Haynes 282, which is known to partition to the $\gamma$ phase and increase the lattice parameter [37]. Goodfellow et al. [38] showed that the lattice misfit of model Ni-based superalloys decreased with increasing Mo content, becoming negative above around 4 at.%.

### 3.2. Macroscopic mechanical response

Representative images of the fine and coarse $\gamma'$ microstructures are shown in Fig. 2(a) and (b), respectively, and the corresponding set of true stress–strain curves for all temperatures are shown in (c) and (d). In general, stress levels decrease with increasing temperature and, as can be seen in Fig. 2(e), the yield strength decreases almost linearly with temperature for both microstructures. The difference in yield strength between the samples remain approximately constant with temperature, being around 100 MPa higher for fine $\gamma'$ as a result of the more effective strengthening associated with particle shearing. The ductility is consistently higher for coarse $\gamma'$, and is only slightly lower at 100 K compared to room temperature, but decreases drastically at 20 K (Fig. 2(e)).

The work hardening rates for the respective microstructures are independent of temperature, see Fig. 2(f) and (g). The fine $\gamma'$ samples show an extended period of gradually decreasing work hardening followed by a slower decrease at higher strains. The work hardening rate of coarse $\gamma'$ shows a more abrupt change from the elasto-plastic transition region to a linear region, defined as stage II work hardening. The behaviour is consistent with previous observations for this alloys [39]. The linear stage II hardening rates agree well with theoretical values $\theta_{II} = M^2\mu/300 - M^2\mu/200$, where $M$ is the Taylor factor (3.06 for fcc materials with random texture) and $\mu$ is the shear modulus. Here we use a shear modulus of 81 GPa [40], and neglect the temperature dependence as results for other Ni-base superalloys suggest that it should be negligible [41]). Similar stage II hardening has been observed at room temperature in other precipitation strengthened Ni-base alloys [42–44], but most extensively studied in X-750 [42]. The linear hardening rate $\theta_{II}$ was shown to increase with particle size for diameters up to around 120 nm, but at larger diameters it decreased to values similar to those observed for small particles (<50 nm) [42]. This is consistent with Fig. 2(f) and (g) where the hardening rates for fine and coarse microstructures are similar at larger strains. Here we also note that SEM and EBSD investigations of the samples deformed at the lowest temperature, 20 K, did not reveal any signs of deformation twinning, and effects of twinning are therefore neglected in the following.

### 3.3. Phase-averaged response

Fig. 3 shows the evolution of the phase-averaged elastic lattice strains. In fine $\gamma'$, Fig. 3(a)-(c), matrix and precipitates deform together at all temperatures, and the elastic lattice strains increase almost linearly with applied stress, without load partitioning between $\gamma$ and $\gamma'$. This is consistent with shearing of particles by pairs of coupled dislocations, which has been shown to occur at room temperature in the present alloy for this particle size [14]. We note that there is a slight difference in response between $\gamma$ and $\gamma'$ at 100 K (Fig. 3(b)), present also in the elastic region, but as will shown later this is due to problems with fitting the very weak (100) superlattice peak.

The coarse $\gamma'$ microstructure, on the other hand, shows significant load partitioning between the phases after the yield point (yellow dashed line), see Fig. 3(d)-(f), associated with looping of dislocations around the coarse particles [14]. While the lattice strains in the $\gamma$ phase increases linearly with applied stress (similar to fine $\gamma'$), the coarse $\gamma'$ particles accommodate a larger share of the load as seen by the rapid accumulation of elastic lattice strains after yielding. The $\gamma'$ lattice strain undergoes two stages after yielding, seen as a change in slope at stress levels around 200 MPa above the yield stress (approximately marked by red arrows in Fig. 3(d)-(f)). The temperature dependent development of the partitioning can be seen in Fig. 4, where the load redistribution (characterised by the partitioning of the phase-averaged elastic lattice strains, $\Delta\epsilon = \epsilon^{\gamma'} - \epsilon^{\gamma}$, is plotted against the increase in stress beyond the yield stress. The rate of load transfer is constant in the initial stage at all temperatures, but decreases at higher strains. The decrease is more pronounced at 100 K compared to 300 K, but at 20 K fracture occurs too early to determine if the behaviour extends to this temperature as well. We will return to the effect of temperature on the load partitioning later, when examining the orientation specific behaviour of the phases.

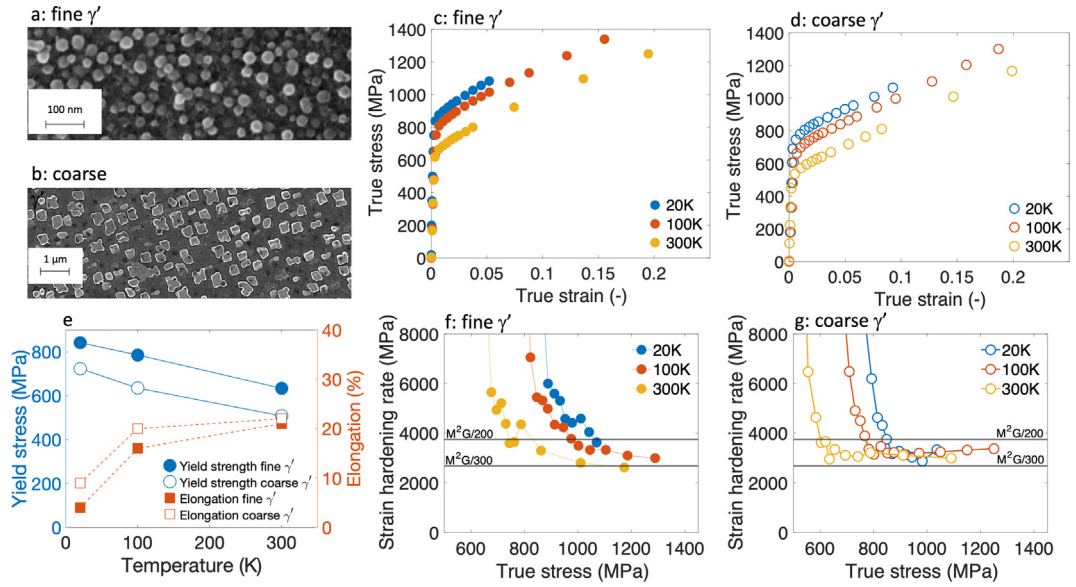


**Fig. 2.** Illustration of two-unimodal microstructures of Haynes 282, (a) fine $\gamma'$ and (b) coarse $\gamma'$. Global stress–strain curves measured at 20 K, 100 K and 300 K with (c) fine $\gamma'$, (d) coarse $\gamma'$ followed by the (e) variation of yield stress and ductility with temperatures for both microstructures. Strain hardening behavior of (f) fine $\gamma'$ and (g) coarse $\gamma'$ microstructures at respective temperatures.

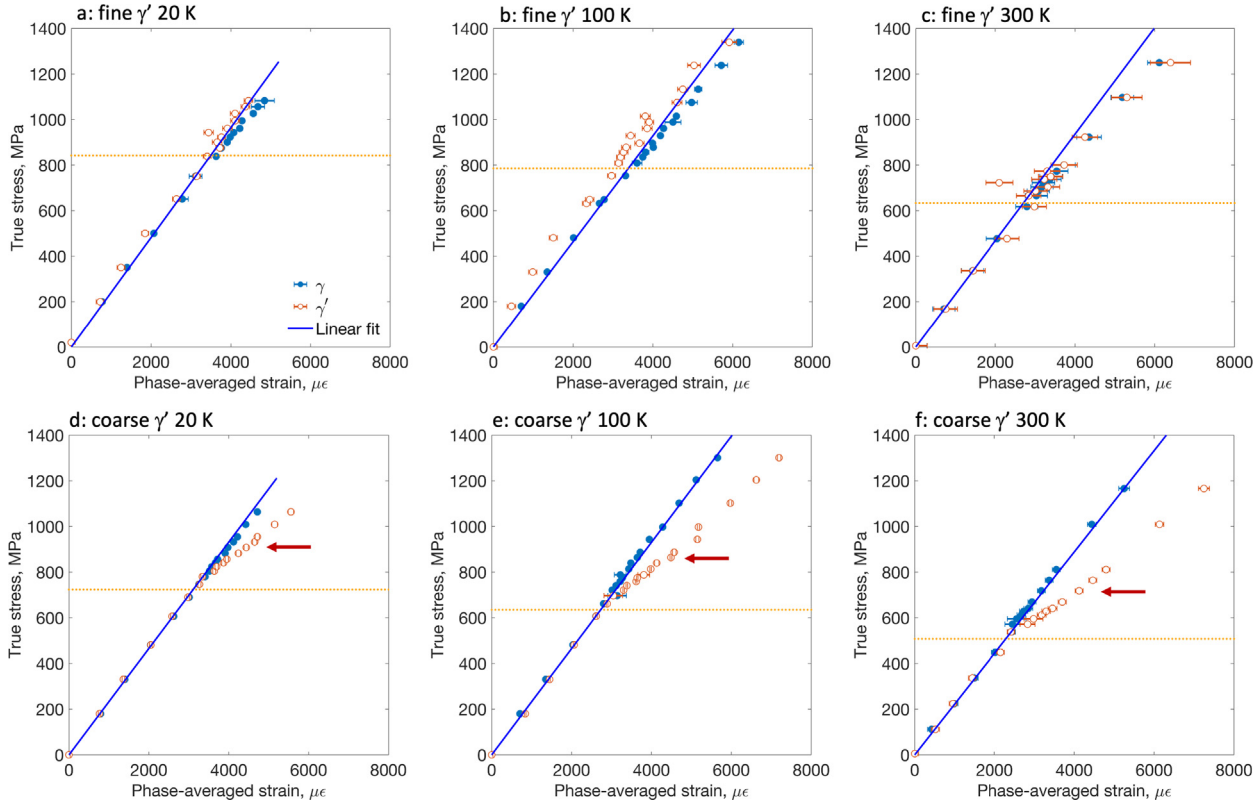


**Fig. 3.** Phase-averaged lattice strains in case of (a-c) fine and (d-f) coarse $\gamma'$ microstructures at (a,d) 20 K, (b,e) 100 K and (c,f) 300 K, respectively. The yellow dashed lines indicate the yield stress and the blue solid lines shows the slope of the $\gamma$ lattice strain evolution in the elastic region. Red arrows in (d-f) indicate approximate stress levels where a change in slope of the elastic lattice strain development can be seen.

### *3.4. Orientation-specific response*

In order to further understand the connections between the macroscopic and the phase-averaged behaviour, we examine the orientation dependence of the lattice strain evolution in grain families with different orientations (i.e. all grains with specific ⟨*hkl*⟩ direction aligned with the tensile axis, measured from the (*hkl*) diffraction peak) for the two phases. Here we must point out that a specific $\gamma$ grain will be subject to elastic interactions with grains of different orientations (*intergranular* interactions), as well as with

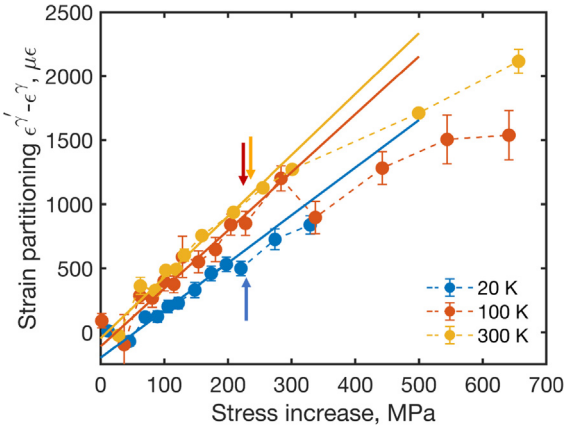


**Fig. 4.** Elastic lattice strain (equivalent to load) partitioning between $\gamma$ and $\gamma'$ as a function of stress increase above the yield stress in the coarse microstructure. Arrows indicate the approximate positions identified in Fig. 3(d)-(f).

the embedded coherent particles inside the grain which share the same orientation (intragranular interaction). The $\gamma'$ particles, on the other hand, only interact (*intragranularly*) with their parent grain but not between themselves or directly with particles with different orientation. During deformation the ⟨111⟩ and ⟨311⟩ oriented grains in the $\gamma$ matrix show very limited changes in slope upon yielding (Fig. 5). This behaviour is common for both coarse and fine $\gamma'$. The ⟨220⟩ oriented grains undergo early yielding (seen as an increase in the slope), which leads to intergranular load transfer to the ⟨200⟩ orientation in the matrix. In the fine $\gamma'$ microstructure, the load transfer in the matrix phase is directly reflected in the strengthening particles seen as an increased accumulation of elastic lattice strains in the ⟨100⟩ orientation (Fig. 6(a)-(c)). Apart from yielding of the ⟨110⟩ orientation, which is necessary due to lattice coherence and particle shearing, also the ⟨210⟩ and ⟨211⟩ orientations in $\gamma'$ show an increase in the slope after the yield stress (Fig. 6(a)-(c)). This suggests that the matrix grains with the same orientation also yield, which is expected due to their high Schmid factor, although the associated diffraction peaks are not available in the current diffractograms. The intergranular load transfer to ⟨200⟩ in the coarse $\gamma'$ microstructure is seen as a partitioning to ⟨100⟩ also in the particles. However, no signs of yielding can be seen in $\gamma'$ at the early stages of deformation, not even in the ⟨110⟩ orientation. Interestingly, there is a pronounced change in slope of ⟨110⟩ at higher stresses (red arrows), indicating that yielding does occur in the later stage of deformation. Yielding of the ⟨110⟩ is not associated with increased load transfer to ⟨100⟩ orientation, which instead also appears to undergo yielding at higher stresses (blue arrows), although less obvious compared to ⟨110⟩.

This situation is more clearly seen in Fig. 7 where the behaviour of the $\gamma'$ superlattice ⟨100⟩ and ⟨110⟩ peaks are directly compared to the corresponding fundamental ⟨200⟩ and ⟨220⟩ peaks from the $\gamma$ matrix. The previously described behaviour is confirmed, where the ⟨100⟩ and ⟨200⟩ in the fine $\gamma'$ samples overlap, as expected from the precipitate shearing induced co-deformation, and increase linearly (Fig. 7(a)-(c)). The ⟨110⟩ and ⟨220⟩ strains also overlap, but clearly exhibit an almost ideally plastic behaviour after yielding followed by a linear development with smaller slope (except at 20 K, due to the early fracture). From Fig. 7(b) we can also note the reason for the previously mentioned separation of the phase-averaged $\gamma$ and $\gamma'$ lattice strains in Fig. 3(b). Whereas the ⟨110⟩ and ⟨220⟩ agree closely, the ⟨100⟩ appear to be off-set from the ⟨200⟩ data points, even in the elastic region. As ⟨100⟩ and ⟨200⟩ agree well at both higher and lower temperatures, and ⟨110⟩ and

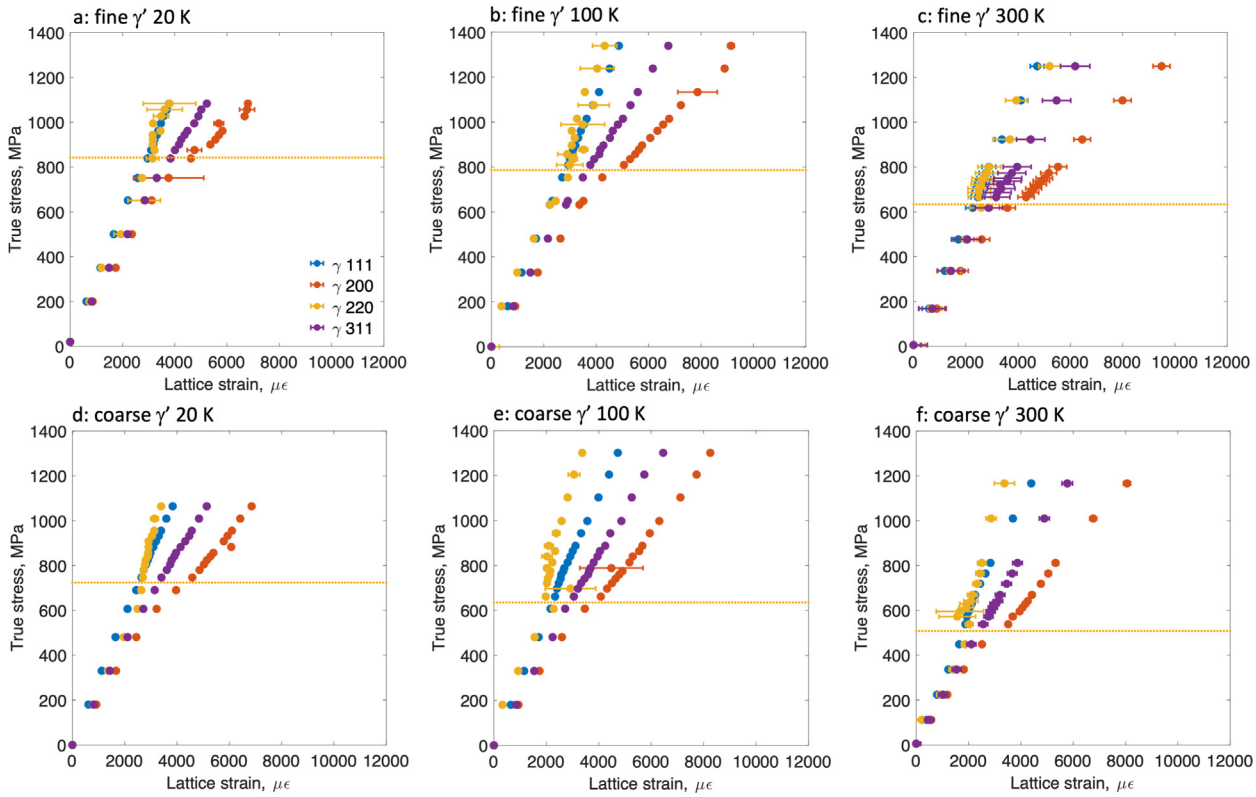


**Fig. 5.** The elastic lattice strains against applied stress of the fundamental FCC peaks of (a-c) fine and (d-f) coarse $\gamma'$ at (a,d) 20 K, (b,e) 100 K and (c,f) 300 K, respectively. The yellow dashed lines indicate the yield stress.

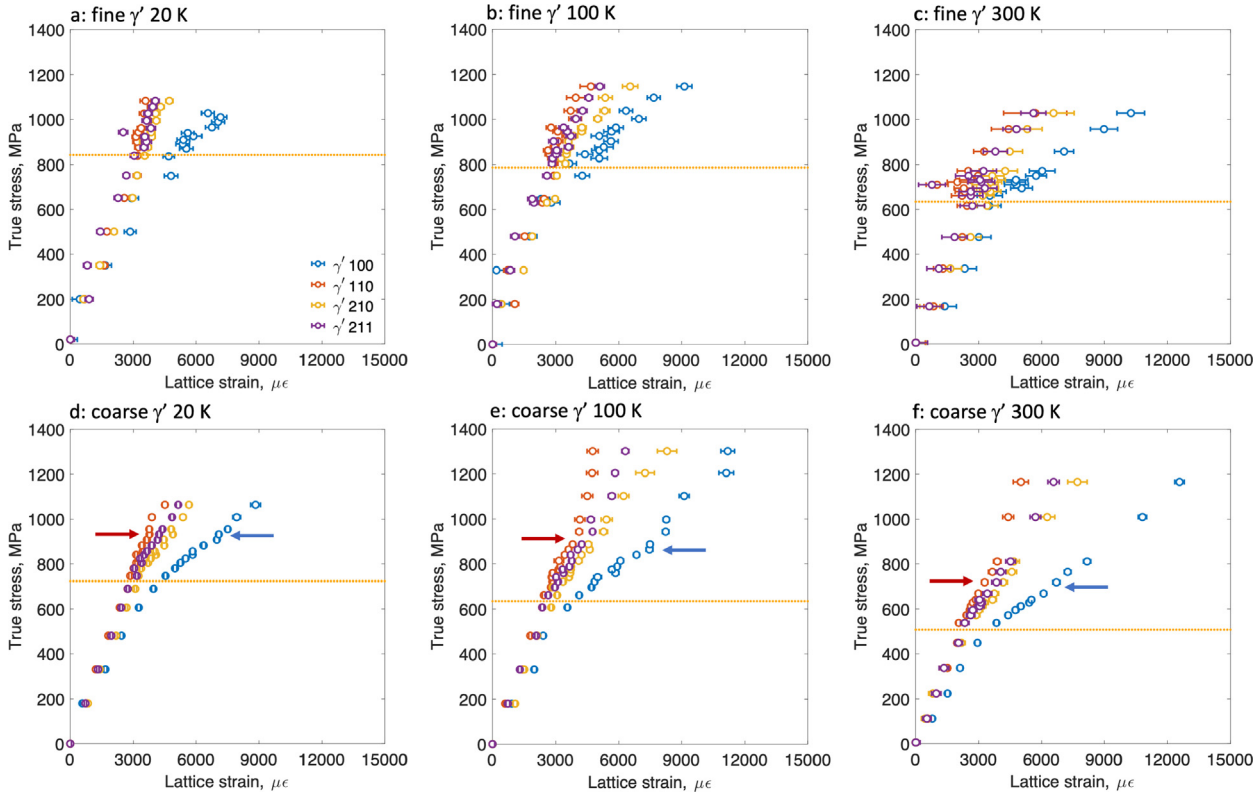


**Fig. 6.** The elastic lattice strains against applied stress of the superlattice $\gamma'$ peaks of (a-c) fine and (d-f) coarse $\gamma'$ at (a,d) 20 K, (b,e) 100 K and (c,f) 300 K, respectively. The yellow dashed lines indicate the yield stress. Blue and red arrows in (d-f) indicate yielding of the <100> and <110> orientations, respectively.

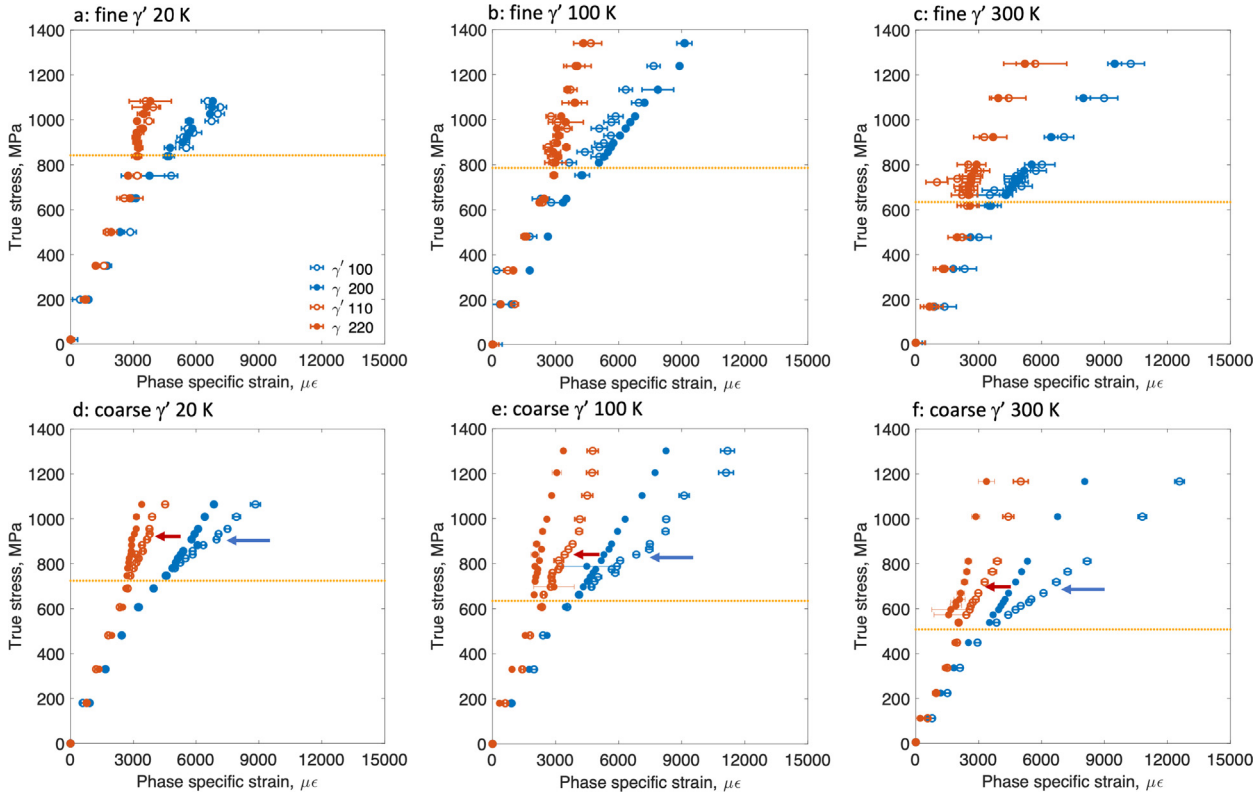


**Fig. 7.** Load distribution between $\gamma'$ <100>/ $\gamma$ <200> and $\gamma'$ <110>/ $\gamma$ <220> in (a-c) fine and (d-f) coarse $\gamma'$ microstructures at (a,d) 20 K, (b,e) 100 K and (c,f) 300 K, respectively. The yellow dashed lines indicate the yield stress. Blue and red arrows in (d-f) indicate yielding of the <100> and <110> orientations, respectively.

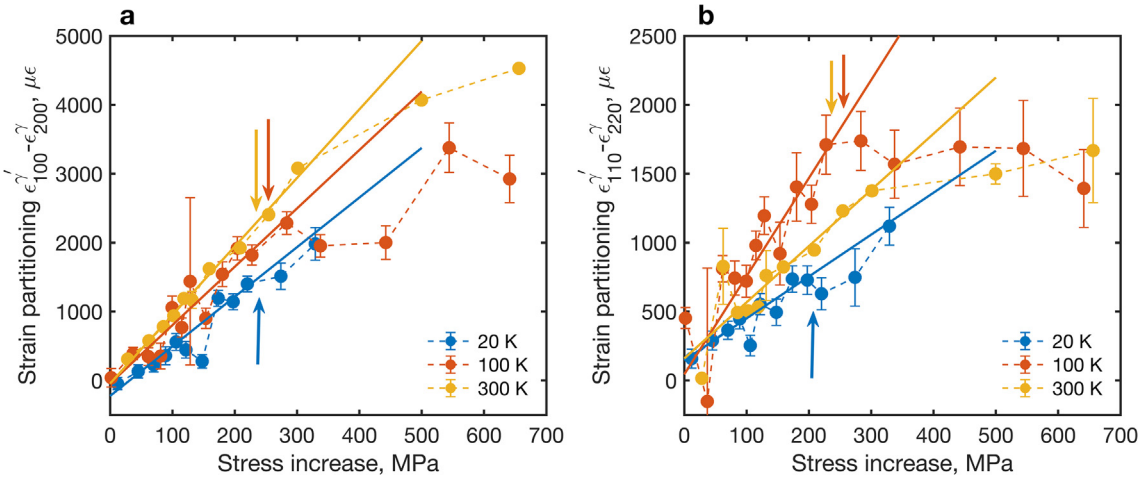


**Fig. 8.** Elastic lattice strain (equivalent to load) partitioning between $\gamma$ and $\gamma'$ for grains with (a) ⟨100⟩/⟨200⟩ orientation and (b) ⟨220⟩/⟨110⟩ orientation parallel to the tensile direction, as a function of stress increase above the yield stress. Arrows mark approximate points identified in Figure 6(d)-(f) and Figure 7(d)-(f).

⟨220⟩ agree at all three temperatures, this is likely an artefact attributed to problems of fitting the smaller ⟨100⟩ peak in the sample tested at 100 K.

The comparison of $\gamma$ and $\gamma'$ lattice strain evolution in the coarse microstructure provides a clearer picture of the load partitioning. At 300 K, the ⟨220⟩ oriented grains yield early and transfer the load to the impenetrable $\gamma'$ ⟨110⟩ oriented particles within the grains. The yielding also leads to intergranular load transfer to the ⟨200⟩ grains which accumulate elastic strain (i.e. load) more rapidly after the yield point. However, intragranular load partitioning occurs also within the ⟨200⟩ oriented grains, from the matrix to the $\gamma'$ particles. The previously described changes in the slope for the ⟨100⟩ and ⟨110⟩ orientations, which was suggested to indicate yielding, occur at a global stress of around 700 MPa, approximately 200 MPa above the yield stress (blue and red arrows, respectively). The situation is similar at 100 K, but the second change in slope occurs at higher stresses (∼800 MPa), corresponding to similar values of the stress increase above yield stress (∼200 MPa). At 20 K similar observations can made, but the early fracture prevents the complete analysis.

Fig. 8 shows the strain partitioning between the two phases in grains with specific orientations. Similar to Fig. 4, the partitioning is defined as $\Delta\epsilon_{hkl} = \epsilon^{\gamma'}_{hkl} - \epsilon^{\gamma}_{hkl}$. Both orientations show approximately constant rate of partitioning for all temperatures in the early stage, but the behaviour at higher stresses is temperature dependent, as discussed above. The ⟨100⟩ orientation show a more pronounced decrease in partitioning rate at 100 K compared to 300 K (Fig. 8(a)). The effect is even more pronounced in the ⟨110⟩ orientation, where the partitioning rate becomes almost independent of applied stress at higher stresses (Fig. 8(b)).

## 4. Conclusions

In summary, we present the first report on microstructure dependent micro-mechanical response of a precipitation strengthened Ni-based superalloy at cryogenic temperatures. In-situ neutron diffraction during tensile testing at 20, 100 and 300 K was used to investigate the orientation and phase-specific response of Haynes 282 with fine (20 nm) and coarse (200 nm) $\gamma'$ particles. From this study we report that:

- The yield strength and elongation are both strongly temperature dependent, whereas the work hardening response of each microstructure is essentially independent of temperature. In particular, the coarse microstructure exhibited linear hardening at all temperatures, consistent with theoretical values of stage II behaviour. Fine particles lead to co-deformation and coarse particles induced load partitioning at all temperatures.
- While the phase-averaged lattice strain in the matrix phase in both coarse and fine microstructures develop linearly with applied stress, pronounced intergranular load partitioning occurs between different orientations *within* the $\gamma$ phase due to elastic interactions. The ⟨200⟩ and ⟨220⟩ orientations deviate most from linearity, with early yielding of the ⟨220⟩ orientation leading to load transfer to ⟨200⟩.
- In the fine microstructure the load transfer to the ⟨200⟩ orientation also leads to accumulation of larger lattice strains in the coherent ⟨100⟩ oriented $\gamma'$.
- The lattice strain in the coarse $\gamma'$ microstructure exhibits a more complex behaviour. As the ⟨220⟩ oriented matrix grains yield early, they *intragranularly* transfer the load to the large impenetrable embedded $\gamma'$ particles and *intergranularly* primarily to the ⟨200⟩ oriented grains. Within the more highly loaded ⟨200⟩ orientation, the load is, in turn, preferentially transferred to the $\gamma'$ particles. At higher stresses the response of the ⟨200⟩ and ⟨220⟩ oriented grains exhibit a change in slope which indicates that the coarse $\gamma'$ do indeed undergo yielding in the later stages of deformation. As a result the rate of load partitioning is approximately constant in the early stages of deformation, but decreases at large strains (high stresses) due to the yielding of $\gamma'$. This effect is more pronounced in the ⟨110⟩ orientation, compared to ⟨100⟩, and appears to increase with decreasing temperatures.

Further understanding of the yielding of $\gamma'$ at high stresses is required, and the phenomenon should be considered in development of models for predicting the effect of impenetrable coherent particles on the mechanical behaviour.

## Funding

This research is funded by the Swedish Foundation for Strategic Research (SSF) within the Swedish National Graduate School in Neutron Scattering (SwedNESS) with Grant No. GSn15–0008.

## Data availability

The raw/processed data required to reproduce these findings cannot be shared at this time due to technical or time limitations.

## Declaration of Competing Interest

The authors declare that they have no known competing financial interests or personal relationships that could have appeared to influence the work reported in this paper.

## Acknowledgements

This research is funded by the Swedish Foundation for Strategic Research (SSF) within the Swedish national graduate school in neutron scattering (SwedNess). The material was supplied by GKN Aerospace Engine Systems, Trollhättan, Sweden. The authors acknowledge the allocation of beam time (RB1720281 and RB1820368) at ISIS Neutron and Muon Source, Rutherford Appleton Laboratory, funded by the Science and Technology Facilities Council.

## Appendix A. Supplementary material

Supplementary data associated with this article can be found, in the online version, at https://doi.org/10.1016/j.matdes.2021.109954.

## References

[1] R.C. Reed, 2 The physical metallurgy of nickel and its alloys, Superalloys-Fundamentals and Applications (2006) 33–120, https://doi.org/10.1017/CBO9780511541285.
[2] M. Daymond, M. Preuss, B. Clausen, Evidence of variation in slip mode in a polycrystalline nickel-base superalloy with change in temperature from neutron diffraction strain measurements, Acta materialia 55 (9) (2007) 3089–3102, https://doi.org/10.1016/j.actamat.2007.01.013.
[3] S. Karthikeyan, R. Unocic, P. Sarosi, G. Viswanathan, D. Whitis, M. Mills, Modeling microtwinning during creep in ni-based superalloys, Scripta Mater. 54 (6) (2006) 1157–1162, https://doi.org/10.1016/j.scriptamat.2005.11.049.
[4] L. Kovarik, R.R. Unocic, J. Li, P. Sarosi, C. Shen, Y. Wang, M.J. Mills, Microtwinning and other shearing mechanisms at intermediate temperatures in Ni-based superalloys, Prog. Mater Sci. 54 (6) (2009) 839–873, https://doi.org/10.1016/j.pmatsci.2009.03.010.
[5] Y. Yuan, Y.F. Gu, T. Osada, Z.H. Zhong, T. Yokokawa, H. Harada, Deformation mechanisms in a new disc superalloy at low and intermediate temperatures, Scripta Mater. 67 (2) (2012) 137–140, https://doi.org/10.1016/j.scriptamat.2012.03.042.
[6] J. Chen, J. Dong, M. Zhang, Z. Yao, Deformation mechanisms in a fine-grained Udimet 720LI nickel-base superalloy with high volume fractions of γ' phases, Mater. Sci. Eng., A 673 (2016) 122–134, https://doi.org/10.1016/j.msea.2016.07.068.
[7] J.J. Moverare, S. Johansson, R.C. Reed, Deformation and damage mechanisms during thermal-mechanical fatigue of a single-crystal superalloy, Acta Mater. 57 (7) (2009) 2266–2276, https://doi.org/10.1016/j.actamat.2009.01.027.
[8] J. Kanesund, J.J. Moverare, S. Johansson, Deformation and damage mechanisms in IN792 during thermomechanical fatigue, Mater. Sci. Eng., A 528 (13–14) (2011) 4658–4668, https://doi.org/10.1016/j.msea.2011.02.063.
[9] F. Sun, J. Zhang, H. Harada, Deformation twinning and twinning-related fracture in nickel-base single-crystal superalloys during thermomechanical fatigue cycling, Acta Mater. 67 (2014) 45–57, https://doi.org/10.1016/j.actamat.2013.12.011.
[10] P. Zhang, Y. Yuan, H. Yin, Y. Gu, J. Wang, M. Yang, G. Yang, X. Song, Tensile Properties and Deformation Mechanisms of Haynes 282 at Various Temperatures, Metall. Mater. Trans. A 49 (5) (2018) 1571–1578, https://doi.org/10.1007/s11661-018-4515-5.
[11] P. Zhang, Y. Yuan, Y. Gu, Y. Dang, J. Lu, X. Zhao, J. Wang, C. Zhu, C. Fan, Temperature dependence of deformation mechanisms and tensile strength of a new Ni-Fe-base superalloy, Mater. Charact. 142 (May) (2018) 101–108, https://doi.org/10.1016/j.matchar.2018.05.032.
[12] M. Preuss, J.Q. da Fonseca, B. Grant, E. Knoche, R. Moat, M. Daymond, The effect of γ' particle size on the deformation mechanism in an advanced polycrystalline nickel-base superalloy, Superalloys 2008: 11th International Symposium on Superalloys (010) (2008) 405–414.
[13] B.M.B. Grant, E.M. Francis, J. Quinta Da Fonseca, M.R. Daymond, M. Preuss, Deformation behaviour of an advanced nickel-based superalloy studied by neutron diffraction and electron microscopy, Acta Mater. 60 (2012) 6829–6841, https://doi.org/10.1016/j.actamat.2012.09.005.
[14] N.R. Jaladurgam, H. Li, J. Kelleher, C. Persson, A. Steuwer, M.H. Colliander, Microstructure-dependent deformation behaviour of a low γ' volume fraction Ni-base superalloy studied by in-situ neutron diffraction, Acta Mater. 183 (2020) 182–195, https://doi.org/10.1016/j.actamat.2019.11.003.
[15] R.L. Tobler, Low temperature effects on the fracture behaviour of a nickel base superalloy, Cryogenics 16 (11) (1976) 669–674, https://doi.org/10.1016/0011-2275(76)90039-4.
[16] N. Suzuki, Low-Cycle Fatigue Characteristics of Precipitation-Hardened Superalloys at Cryogenic Temperatures, J. Test. Eval. 28 (4) (2000) 257–266, https://doi.org/10.1520/jte12103j.
[17] Y. Ono, T. Yuri, H. Sumiyoshi, E. Takeuchi, S. Matsuoka, T. Ogata, High-Cycle Fatigue Properties at Cryogenic Temperatures in Inconel 718 Nickel-based Superalloy, Mater. Trans. 45 (2) (2004) 342–345, https://doi.org/10.2320/matertrans.45.342.
[18] Y. Ono, T. Yuri, H. Sumiyoshi, E. Takeuchi, S. Matsuoka, T. Ogata, High-cycle fatigue properties at cryogenic temperatures in inconel 718, in: AIP Conference Proceedings, Vol. 824, American Institute of Physics, 2006, pp. 184–191. doi:10.1063/1.2192350.
[19] R. Jewett, J. Halchak, The Use of Alloy 718 in the Space Shuttle Main Engine, in: Superalloys 718, 625 and Various Derivatives (1991), TMS, 1991, pp. 749–760. doi:10.7449/1991/Superalloys_1991_749_760.
[20] S. Patel, J. DeBarbadillo, S. Coryell, Superalloy 718: Evolution of the Alloy from High to Low Temperature Application, in: Minerals, Metals and Materials Series, Vol. 2018-June, 2018, pp. 23–49. doi:10.1007/978-3-319-89480-5_2.
[21] V. Barabash, A. Peacock, S. Fabritsiev, G. Kalinin, S. Zinkle, A. Rowcliffe, J.W. Rensman, A.A. Tavassoli, P. Marmy, P.J. Karditsas, F. Gillemot, M. Akiba, Materials challenges for ITER - Current status and future activities, Journal of Nuclear Materials 367-370 A (SPEC. ISS.) (2007) 21–32, https://doi.org/10.1016/j.jnucmat.2007.03.017.
[22] S. Jiang, D. Sun, Y. Zhang, X. Zhu, M. Wang, C. Zhao, Plastic deformation mechanisms of NiCuCrMoTiAlNb Ni-based alloys at cryogenic temperature, Materials Science and Engineering: A 664 (2016) 135–145, https://doi.org/10.1016/j.msea.2016.03.133.
[23] J. Nordström, R. Siriki, M. Calmunger, J. Moverare, G. Chai, TWIP and fracture behavior in the superalloy 625 at room and cryogenic temperatures, Procedia Structural Integrity 23 (2019) (2019) 457–462, https://doi.org/10.1016/j.prostr.2020.01.129.
[24] Q. Ding, H. Bei, X. Wei, Y. Gao, Z. Zhang, Nano-twin-induced exceptionally superior cryogenic mechanical properties of a Ni-based GH3536 (Hastelloy X) superalloy, Materials Today Nano 14 (2021) 100110, https://doi.org/10.1016/j.mtnano.2021.100110.
[25] Air Force Materials Laboratory AFML-TDR-64-280: Cryogenic Materials Data Handbook, Tech. rep. (1970).
[26] L.M. Pike, HAYNES 282 Alloy: A New Wrought Superalloy Designed for Improved Creep Strength and Fabricability, in: Volume 4: Cycle Innovations; Electric Power; Industrial and Cogeneration; Manufacturing Materials and Metallurgy, ASME, 2006, p. 1031. doi:10.1115/GT2006-91204.
[27] J.R. Santisteban, M.R. Daymond, J.A. James, L. Edwards, ENGIN-X: A third-generation neutron strain scanner, J. Appl. Crystallogr. 39 (2006) 812–825, https://doi.org/10.1107/S0021889806042245.
[28] O. Kirichek, J.D. Timms, J.F. Kelleher, R.B. Down, C.D. Offer, S. Kabra, S.Y. Zhang, Sample environment for neutron scattering measurements of internal stresses in engineering materials in the temperature range of 6 K to 300 K, Rev. Sci. Instrum. 88 (2) (2017) 025103, https://doi.org/10.1063/1.4974815.
[29] Y. Wang, B. Liu, K. Yan, M. Wang, S. Kabra, Y.L. Chiu, D. Dye, P.D. Lee, Y. Liu, B. Cai, Probing deformation mechanisms of a FeCoCrNi high-entropy alloy at 293 and 77 K using in situ neutron diffraction, Acta Mater. 154 (2018) 79–89, https://doi.org/10.1016/j.actamat.2018.05.013.
[30] L. Tang, L. Wang, M. Wang, H. Liu, S. Kabra, Y. Chiu, B. Cai, Synergistic deformation pathways in a TWIP steel at cryogenic temperatures: In situ neutron diffraction, Acta Mater. 200 (2020) 943–958, https://doi.org/10.1016/j.actamat.2020.09.075.
[31] L. Tang, K. Yan, B. Cai, Y. Wang, B. Liu, S. Kabra, M.M. Attallah, Y. Liu, Deformation mechanisms of FeCoCrNiMo0.2 high entropy alloy at 77 and 15 K, Scripta Mater. 178 (2020) 166–170, https://doi.org/10.1016/j.scriptamat.2019.11.026.
[32] Y. Shi, S. Li, T.L. Lee, X. Hui, Z. Zhang, R. Li, M. Zhang, S. Kabra, Y.-D. Wang, In situ neutron diffraction study of a new type of stress-induced confined martensitic transformation in Fe22Co20Ni19Cr20Mn12Al7 high-entropy alloy, Materials Science and Engineering: A 771 (2020) 138555, https://doi.org/10.1016/j.msea.2019.138555.
[33] B.H. Toby, R.B. Von Dreele, IUCr, GSAS-II: the genesis of a modern open-source all purpose crystallography software package, J. Appl. Crystallogr. 46 (2) (2013) 544–549, https://doi.org/10.1107/S0021889813003531.
[34] M.R. Daymond, The determination of a continuum mechanics equivalent elastic strain from the analysis of multiple diffraction peaks, J. Appl. Phys. 96 (8) (2004) 4263–4272, https://doi.org/10.1063/1.1794896.
[35] A. Clark, Low temperature thermal expansion of some metallic alloys, Cryogenics 8 (5) (1968) 282–289, https://doi.org/10.1016/S0011-2275(68)80003-7.
[36] J.A. Hawk, T.-L. Cheng, J.S. Sears, P.D. Jablonski, Y.-H. Wen, Gamma prime stability in haynes 282: theoretical and experimental considerations, J. Mater. Eng. Perform. 24 (11) (2015) 4171–4181.
[37] A.K. Jena, M.C. Chaturvedi, The role of alloying elements in the design of nickel-base superalloys, J. Mater. Sci. 19 (10) (1984) 3121–3139, https://doi.org/10.1007/BF00549796.
[38] A. Goodfellow, J. Kelleher, N. Jones, D. Dye, M. Hardy, H. Stone, The effect of Mo on load partitioning and microstrain evolution during compression of a series of polycrystalline Ni-Based superalloys, Acta Mater. 176 (2019) 318–329, https://doi.org/10.1016/j.actamat.2019.07.002.

[39] C. Joseph, C. Persson, M. Hörnqvist Colliander, Influence of heat treatment on the microstructure and tensile properties of Ni-base superalloy Haynes 282, Mater. Sci. Eng., A 679 (2017) 520–530, https://doi.org/10.1016/j.msea.2016.10.048.
[40] HAYNES 625 alloy, Haynes International, Tech. rep. (2017). URL https://www.haynesintl.com/docs/default-source/pdfs/new-alloy-brochures/high-temperature-alloys/brochures/282-brochure.pdf?sfvrsn=20
[41] INCONEL ALLOY 718, Special metals, Tech. rep. (2007). URL https://www.specialmetals.com/assets/smc/documents/inconel_alloy_718.pdf
[42] J. Del Valle, A. Picasso, R. Romero, Work-hardening in Inconel X-750: study of stage II, Acta materialia 46 (6) (1998) 1981–1988, https://doi.org/10.1016/S1359-6454(97)00425-4.
[43] K. Praveen, G. Sastry, V. Singh, Work-hardening behavior of the Ni-Fe based superalloy IN718, Metallurgical and Materials transactions A 39 (1) (2008) 65–78, https://doi.org/10.1007/s11661-007-9375-3.
[44] J. Mittra, J. Dubey, U. Kulkarni, G. Dey, Role of dislocation density in raising the stage II work-hardening rate of Alloy 625, Materials Science and Engineering: A 512 (1–2) (2009) 87–91, https://doi.org/10.1016/j.msea.2009.02.053.